DFT-Computed Trends in the Properties of Bimetallic Precious-Metal Nanoparticles with Core@Shell Segregation

Andrew J. Logsdail,*,† Lauro Oliver Paz-Bórbon,‡ and Christopher A. Downing¶

Cardiff Catalysis Institute, Cardiff University School of Chemistry, Main Building, Park Place, Cardiff, CF10 3AT, UK, Instituto de Física, Universidad Nacional Autónoma de México, Apartado Postal 20-364, México DF 01000, México, and University College London, Kathleen Lonsdale Materials Chemistry, Department of Chemistry, 20 Gordon St., London, WC1H 0AJ, UK

E-mail: LogsdailA@cardiff.ac.uk

Abstract

Bimetallic precious-metal nanoparticles (NPs) are promising as components of heterogeneous catalytic systems, however the synergistic effects that occur when combining multiple elements in these discrete systems are still being understood. Here, we present a systematic computational study that investigates the effect of geometry and compositional arrangements on the properties of bimetallic core@shell precious-metal NPs. Combinations of the elements Ag, Au, Pd and Pt are considered and, for surface coverages of just one monolayer,

*To whom correspondence should be addressed

†Cardiff Catalysis Institute, Cardiff University School of Chemistry, Main Building, Park Place, Cardiff, CF10 3AT, UK

‡Instituto de Física, Universidad Nacional Autónoma de México, Apartado Postal 20-364, México DF 01000, México

¶University College London, Kathleen Lonsdale Materials Chemistry, Department of Chemistry, 20 Gordon St., London, WC1H 0AJ, UK

we show that the electronic properties of the NP, such as the Fermi energy and d-band centre, are strongly correlated with the element occupying sites at the NP surface, in qualitative but not quantitative agreement with previous two-dimensional slab calculations. In contrast, strain effects from structural choices and elemental size mismatch play a minor role in altering energetic levels. Charge transfer between the core and shell regions of the NPs is a balance between the increased electronic degrees of freedom that implicitly exists at an NP surface and the electronegativity of the constituent elements, with Au and Ag respectively good and bad at retaining electron density. We use our results to rationalise recent experimental observations, and foresee that the outcomes will assist the rational atom-by-atom design of future nanoparticle catalysts.

1 Introduction

Metallic nanoparticles (NPs) offer great promise for applications in chemical sciences due to their novel properties when compared to bulk or atomic counterparts. Since the first reports of the reactivity of gold NPs by Haruta[1] and Hutchings,[2] applications of precious-metal NPs have become widespread through catalysis,[3–8] electronics[9–11] and optics.[12–14] However, the scarcity and high-cost of Au and Pt demands a shift towards improvements in the design and controlled synthesis of precious-metal NPs.[15] The use of bimetallic NPs, where two metals are combined, has thus proven an excellent method for reducing costs whilst improving the catalytic chemistry feasible with NPs.[15–18] Size, structure and chemical arrangements of the bimetallic NPs can be experimentally controlled through careful synthesis protocols,[19,20] which allows fine tuning and maximisation of the the synergistic benefits available when combining multiple elements.[17] Bimetallic NPs can be categorised broadly as having alloy, janus-segregated or core@shell chemical arrangements, with the latter particularly appealing for catalysis as it is relatively facile to synthesise, with e.g. sequential precipitation, and a reactive "first-choice" metal can be supported on a core of an alternative cheaper material, lowering the manufacturing cost of the catalyst and potentially improving turnover frequencies due to compositional synergy.[21–25]

The discrete nature of NPs lends themselves towards computational modelling techniques where forcefield or quantum mechanical methods can elucidate fundamental properties.[17] Many comprehensive computational investigations have been considered for bimetallic NPs, or "nanoalloys",[16,17] with emphasis on exploring either: (i) the structure, chemical arrangement and properties of energetic minima;[17,26–31] or (ii) the surface reactivity of idealised structures.[32–36] Whilst the extrapolation of properties for single-element systems to large NP sizes are well established,[37,38] the same process is complicated for bimetallic NPs by the additional compositional parameters. Similarly, the relationship of catalytic observables, such as reactivity, to the position of the d-band centre[39–44] or structural features, such as edges and vertices,[45,46] have been investigated thoroughly for monometallic NPs, but bimetallic NPs are structurally and compositionally more complicated;[47] too simplify the analysis, d-band positioning, and chemical interactions, are often considered using periodic slab models with dopants and/or monolayer coverages of a secondary element probing the property changes.[23,25,48] For unrelaxed slab models, Ruban *et al.* documented shifts in the d-band centre for a range of transition metals;[49] the effect of epitaxial strain on d-band chemistry has been generalised since for bimetallic surfaces,[50,51] with the width of the surface d-band noted as being responsive to structural factors, and the d-band centre downshifting in response to band broadening. Such effects have been correlated to CO chemisorption on to Pt- and Pd-coated Au surfaces by Pedersen *et al.*[52] and Roudgar *et al.*,[53] respectively.

Despite the range of work covering bimetallic bulk surfaces, the properties of bimetallic NPs remain less thoroughly studied. Tang and Henkelman showed that the binding energy of atomic oxygen correlates to d-band levels of the surface layers in M@Pd NPs, where M ranged over Mo, Co, Cu, Ag, Au and Pd. In particular, noble metal cores (Ag, Au) resulted in an upshift in the surface d-band states, which led to stronger surface binding of the O species.[54] The authors note that strain affects the position of the d-band centre in the NPs, but structural relaxation minimises this effect when compared to single-crystal (i.e. slab) surfaces, at which point the redistribution of electron density has a greater influence. However, Gorzkowski and Lewera recently reported a disagreement between experiment and d-band theory for formic acid decomposition over Pd-core

Pt-shell (Pd@Pt) nanoparticles,[55] which was attributed to changes in the density of states close to the Fermi level rather than the overall d-band width. Similarly, formic acid decomposition over M@Pd NPs (M = Rh, Ru, Ag, Au, Pd, Pt) was correlated with influencing factors beyond the standard d-band model, focusing instead on the work function of the core element, with Ag being most effective, and surface charge accumulation used as rationale for the experimental results.[56] In contrast, Holmberg *et al.* produced recently an investigation of the Fermi energy (ε_f) position for bimetallic AuAg nanoparticles, finding this was simply an average of ε_f for monometallic systems weighted by the percentage of the surface covered by each elemental species, e.g. ε_f for Au@Ag would be the same as for a purely Ag NP.[57] This behaviour was attributed to charge equilibration across the bimetallic interface, and noted as being analogous to Vegard's law for the lattice parameter of binary bulk systems,[58] which opens up questions as to: (i) whether other attributes of NPs are similarly dependent on the surface coverage by a particular element; and (ii) whether these properties are affected by NP geometry.

To address some of the inconsistencies reported, and gaps in the literature with respect to the d-band model for discrete bimetallic NPs, we have performed a density functional theory (DFT) investigation of the energetic and electronic properties for core@shell segregated bimetallic NPs, composed of the elements Ag, Au, Pd and Pt. We focus on NPs with 147-atoms, which allows us to exclude spurious "quantum effects". We study a range of structural motifs from close-packed through to bulk fragments, which allows us to compare the structure-dependent properties for elementally equivalent systems. As for the periodic slab models highlighted from previous investigations, the chemical arrangement of the constituent elements affects electronic observables and we discuss our observations with respect to the recent experimental and theoretical results outlined.

2 Methodology

2.1 Structural Definitions

Three high-symmetry, 12-vertex geometries have been considered throughout this work, namely the icosahedron (Ih), Ino-decahedron (I-Dh) and cuboctahedron (CO). Each of these motifs has the same "magic number" nuclearities given by the third-order polynomial:[59]

$$N(k) = \frac{1}{3}[10k^3 + 15k^2 + 11k + 3] \tag{1}$$

where k is the number of shells in the structure; the first few values of N ("magic numbers") in this sequence are 13, 55, 147, 309 and 561. Increasing k leads to larger N but a lower proportion of surface atoms, as explained via the liquid drop model.[60] The Ih, I-Dh and CO structures have distinct atomic arrangements, which leads to differing geometrical attributes (Figure 1). The Ih consists of 20 (111) faces, making it the most spherical of the three structures. This arrangement minimises the surface area to volume ratio whilst maximising nearest neighbours contact, at the expense of higher internal strain.[61] The Ih is energetically most stable for small clusters, where the energy penalty of the large surfaces is too great unless exceptional electronic configurations exist.[62] The minimisation of internal strain is more important for large clusters: The CO, with 8 (111) faces and 6 (100 faces), is a fragment of an FCC crystal and therefore internal strain is at its lowest, meaning that CO is energetically preferable as $N \to \infty$.[62] The I-Dh motif occupies the transitional space between these two geometries, with its structure not containing the tight packing of the Ih structure nor the FCC crystalline structure of the CO: it has 10 (111) faces and 5 (100) faces.

In the following work, calculations have been performed on the Ih, I-Dh and CO structures with $N = 147$. We have focused on model systems so as to characterise the effect of core@shell segregation on NP properties. Thus, we have only considered local, rather than global optimisation for structures. This can be rationalised by considering how the formation and stabilisation

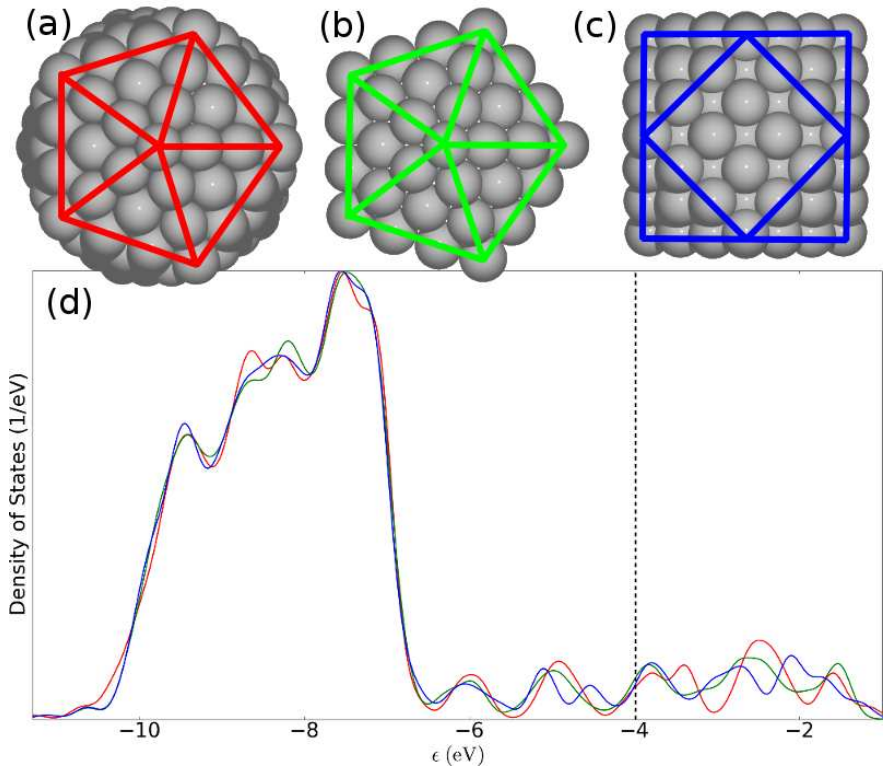

Figure 1: Views of the structural motifs investigated in this work: (a) Icosahedron (Ih), with the (111) faces defined in red; (b) Ino-Decahedron (I-Dh), with the (111) faces defined in green; (c) Cuboctahedorn, with the (100) and (111) faces defined in blue. The total density of states for Ag_{147} NPs with these different structures are presented in (d), relative to a vacuum level of 0 V, with the colours of the plots matched to the structures defined in (a) - (c) i.e. Ih = red, I-Dh = green and CO = blue. The Fermi energy, E_f, relative to vacuum, is marked by a dashed vertical black line; this was calculated as -3.99, -3.99 and -4.00 eV for the Ih, I-Dh and CO, respectively.

of structures with varied geometry and chemical segregation can be performed in experimental synthesis, due to e.g. kinetic trapping[63–66] and ligand-induced surface stabilisation.[17,67,68] The range of structures considered allows us to identify variations with respect to topology as well as composition.

2.2 Computational Methods

Energy calculations were performed using density functional theory (DFT), as implemented in the real-space finite-difference DFT code GPAW.[69,70] GPAW uses the all-electron density, where the core electrons are described using the projector augmented wave (PAW) in the frozen core approximation,[71] with the setup based on a scalar-relativistic spin-paired all-electron calculation. The PAW setup has recently been shown to be the most suitable ionic-core method for calculating the properties of large NPs as an alternative to more computationally-exhaustive all-electron calculations.[72]

Only the valence electrons are treated explicitly in our calculations, via soft pseudo valence wavefunctions; for Ag and Au, this constitutes the outermost 11 electrons ($4d^{10}5s^1$ and $5d^{10}6s^1$ configurations, respectively), whilst for Pd and Pt the outermost 10 electrons are included ($4d^{10}$ and $5d^{10}$, respectively). The Kohn-Sham wavefunctions are expanded directly on a real space grid, with spacing of 0.18 Å, and the Hamiltonian is diagonalised after each geometry step using the RMM-DIIS eigensolver.[73] The generalised gradient approximation (GGA) of Perdew, Burke and Ernzerhof (PBE)[74] is used for the exchange-correlation (XC) energy functional. Fermi-Dirac smearing of 0.1 eV was used to aid self-consistent field (SCF) convergence. No boundary conditions were imposed and therefore all orbital energies are relative to the vacuum level (0 V). The structure of bulk metals are calculated using a primitive FCC unit cell and a $14 \times 14 \times 14$ **k**-point mesh, with all other parameters as outlined above. Lattice parameters were minimised with respect to energy using an equation of state.

Structural optimisation was performed using a quasi-Newtonian (BFGS) method[75] until the maximum force on all atoms is below 0.01 eV/Å, and the total energy change between steps is less

than 10^{-4} eV. The Kohn-Sham orbitals are re-optimised after each ionic step, via self-consistent evaluation, until the change in density is less than 10^{-5} electrons per valence electron and the integrated square of the residuals of the Kohn-Sham equations is less than 10^{-8} per state. Charge redistribution is calculated using Bader charge analysis as implemented by Tang et al.[76] All density of states (DOS) are computed by directly projecting the wavefunctions on to atomic orbitals, centred at the atomic coordinates of the optimised geometries.

2.3 Structural Analysis

The strain at each atomic site was calculated by considering the deformation of bonds in bimetallic NPs compared to the equivalent monometallic systems, with results averaged as a function of like atom species. The strain is expressed as a percentage of the total deformation:

$$e = \frac{l - L}{L} \tag{2}$$

where L and l are the initial and final lengths of the bond of interest. With this notation, contraction of the bond leads to compressive strain whilst extension gives tensile strain.

2.4 Energetic Analysis

The binding energy per atom (E_b) for a bimetallic cluster of composition $X_{N-m}Y_m$ is defined as:

$$E_b = -\frac{E_{tot} - (N-m)E_X - mE_Y}{N} \tag{3}$$

where E_{tot} is the total energy of the system, N is the total number of atoms, m is the number of atoms of element Y, and E_X and E_Y are the energies of the gas-phase atoms X and Y, respectively; $m = 0$ for a monometallic system. Our definition is such that a more positive number indicates stronger binding and, at the bulk limit ($N \to \infty$), our E_b therefore relates to the bulk cohesive energy (E_{coh}) as $E_{coh} = E_b$.

E_{tot}, as reported in GPAW, is relative to the energy of the reference gas-phase atoms (E_X and E_Y) calculated in a spin-paired and spherically symmetric state when generating the PAW setup. However, the energy of the considered gas-phase atoms are dependent on their spin-state and the calculation setup, and this is particularly important for Ag and Au, where $S = \frac{1}{2}$ in the ground state. Thus, the ground-state energies of the gas-phase atoms are calculated to be -0.19, -0.24, -0.04 and -0.32 eV relative to the spin-paired and spherically symmetric reference state for Ag, Au, Pd and Pt, respectively.

2.5 Electronic Analysis

The energy of the highest occupied molecular orbital (ε_{HOMO}) and lowest unoccupied molecular orbital (ε_{LUMO}) are provided relative to the vacuum (0 V), having been taken directly from the eigenvalues at the end of the self-consistent calculation. The Fermi energy (ε_f) is also reported where appropriate: this includes smearing effects and indicates the level at which the orbitals are equiprobable of containing an electron. The difference between ε_{HOMO} and ε_{LUMO} is known as the energy gap, ε_g. The centre of mass for the d-electrons, $\bar{\varepsilon}_d$, is analogous to the d-band centre for bulk[41] and given by:[33]

$$\bar{\varepsilon}_d = \int_{-\infty}^{\varepsilon_{HOMO}} \frac{\rho_d(\varepsilon)}{\rho_d} d\varepsilon - \varepsilon_{HOMO} \tag{4}$$

where ε is the eigenvalue of an electronic state, $\rho_d(\varepsilon)$ is the density of d-electrons for this particular eigenvalue, and ρ_d is the total number of d-electrons. "Core" and "shell" atomic subsets of the total systems were also identified by applying Eq. (4) explicitly to the projected orbitals centred on these atoms, giving values for $\bar{\varepsilon}_{d,core}$ and $\bar{\varepsilon}_{d,shell}$, respectively.

3 Results

3.1 Monometallic NPs

Structural, energetic and electronic results have been thoroughly investigated previously for 147-atom Ag, Au, Pd and Pt NPs[61,63] and are therefore only discussed briefly here, with full analysis provided in the Supporting Information (SI). In general, E_b does not vary significantly with structure, being greatest for the Ih and a difference of less than 0.03 eV/atom for the CO and I-Dh. E_b is ordered Pt (5.03 eV) $>$ Pd (3.08 eV) $>$ Au (2.59 eV) $>$ Ag (2.17 eV) for the Ih structures, which is consistent with the bulk ordering (5.83, 3.75, 3.01 and 2.56 eV, respectively). E_b matches experiment for Pd and Pt, reported as 5.84 and 3.89 eV, respectively,[77] but not for Au (3.81 eV) and Ag (2.95 eV) due to bond-lengthening effects at the GGA level of theory.[78,79]

The ordering of ε_{HOMO} inversely correlates with E_b, as Ag (-4.05) $>$ Au (-4.83 eV) $>$ Pd (-4.89 eV) $>$ Pt (-5.36 eV) for the Ih motif. The variation in ε_{HOMO} for the other geometries was smaller than 0.13 eV. ε_{HOMO} The bulk workfunction (Φ) can be related to our observables via Koopmans' theorem[80,81] as $\Phi = -\varepsilon_{HOMO}$. Φ is the energy required to remove an electron from a system and can depend on surface geometry, ranging between 4.52 and 4.74 eV for bulk Ag (110) and (111) surfaces; between 5.31 and 5.47 eV for Au (111) and (100) surfaces; between 5.22 and 5.6 eV for Pd polycrystalline and (111) surfaces; and between 5.64 and 5.93 eV for the Pt polycrystalline faces, respectively.[82] Our results for NPs are less than the bulk values by ≈ 0.5 eV, which we believe is an effect of quantum confinement i.e. the discretisation of the electronic energy levels.

3.2 Bimetallic NPs

3.2.1 Structural and Energetic Properties

E_b for the bimetallic NPs (Table 1) can be related to the monometallic results through Vegard's law, which dictates that properties of a mixed system will be linearly dependent on the properties of the constiuent elements.[58] For example, combining Pt with Ag reduces E_b(Ih) from 5.03 eV/atom

(monometallic) to 3.85 and 3.32 eV/atom for Ag@Pt and Pt@Ag, respectively, with monometallic Ag being 2.17 eV/atom. More interesting is the stability hierarchy of the structures as we vary the chemical arrangements, with data for all structures given in the SI. In general, Ih is most stable for all systems with an Ag core (Ag@M), and for an Ag shell with a Pd or Pt core (Pd@Ag and Pt@Ag); and the CO is most stable for Au@Ag, Au@Pd and Pt@Pd. The I-Dh is not preferable for *any* of the bimetallic nanopartices - it is joint lowest for only Pt@Pt, Ag@Pd, Au@Pd.

Table 1: Highest binding energy (E_b) for monometallic and bimetallic core@shell NPs. The element in the core (shell) of the NP is presented on the left (top). The values are taken for the highest E_b, i.e. strongest bonded system, which was the Ih motif except for values given in bold, namely those of Au@Ag, Au@Pd and Pt@Pd

	Ag	Au	Pd	Pt
Ag	2.17	2.47	2.48	3.85
Au	**2.33**	2.59	**2.80**	3.93
Pd	2.50	2.90	3.08	4.30
Pt	3.32	3.59	**3.86**	5.03

Instability for the Ih is sometimes related to excessive internal strain from shortened internal bonds (Figure 2), where the strain can be reduced by positioning a smaller element in the core for bimetallic systems;[83–85] considering our elements of interest, Pd and Pt, of Group 10, have experimental (DFT) bond lengths of 2.76 and 2.81 Å, respectively, with errors of $\pm$0.01 Å, whereas Ag and Au, of Group 11, have bond lengths (with similar errors) of 2.88 and 2.96 Å, respectively.[82] Thus, the Ih core@shell could be rationalised as potentially particularly stable for (Group 10)@(Group 11) configurations, with the inverse being the lease stable. However, this hypothesis of instability when the larger element is in the NP core is only valid for Au@Pd (Figure 2), where the CO structure relieves internal strain; unaccounted charge transfer effects influence stability for other compositions. We note that the stronger binding element is at the core of the structure for other compositions favouring CO motifs (Au@Ag and Pt@Pd) and thus we suggest that the FCC fragment facilitates ideal bond lengths for the stronger element (Figure 2), resulting in stronger overall binding for the CO motif.

Calculation of the strain for the core (e_{core}) and shell (e_{shell}) components of the system, as

presented in Figure 3, confirms there is an inverse correlation between core and shell strain for most structures; however, whilst for Ih and I-Dh motifs there is typical not net gain in strain, net positive strain is observed for CO, with the most prominent outliers being CO structures with Ag shells, namely Au@Ag, Pd@Ag and Pt@Ag. We tentatively associate this observation with the interatomic distances in the pure Ag nanoparticle being heavily contracted at specific sites on the CO surface, such as vertices, as seen in Figure 2; however, this cannot be the complete explanation as the effect is observed irrespective of the size of the element in the nanoparticle core, for both smaller (Pd, Pt) and larger (Au) species, and so electronic effects may also play a role.

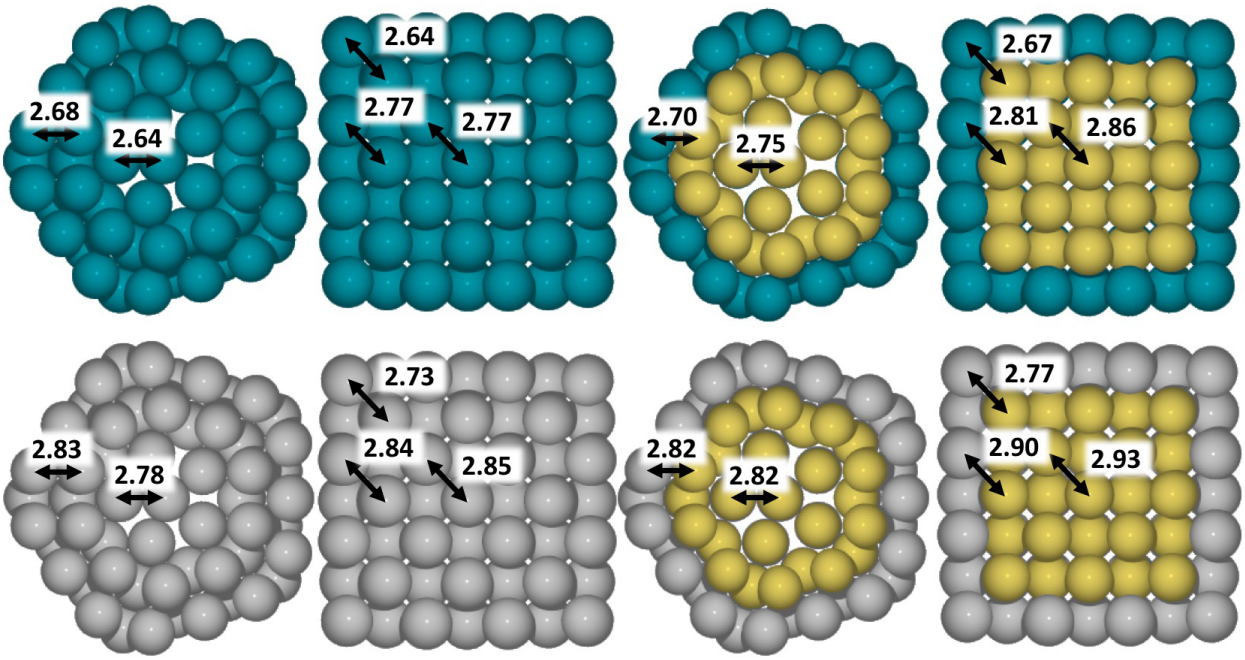

Figure 2: Cutplane views through the middle of monometallic and bimetallic core@shell structures with the internal bond lengths highlighted. Top, left to right: Pd_{147} (Ih); Pd_{147} (CO); $Au_{55}@Pd_{92}$ (Ih); $Au_{55}@Pd_{92}$ (CO). Bottom, left to right: Ag_{147} (Ih); Ag_{147} (CO); $Au_{55}@Ag_{92}$ (Ih); $Ag_{55}@Pd_{92}$ (CO). Ag, Au and Pd atoms are illustrated in silver, gold and blue, respectively. Bond lengths, given in Å, are highlighted in red for specific internal bonds to show the difference in interaction distance in the core and shell regions.

More generally, three clustering of data points is observed in Figure 3, which can be attributed to the relative E_b of the monometallic systems. For systems where the element on the nanoparticle shell has a higher E_b than the core element, compression of the core and expansion of the shell is observed; for the inverse, with the strongest binding element in the core, expansion is observed in

the core in order for the system to maximise the energy available from these stronger bonds. Such behaviour is most prominent for Pt, and to a lesser degree Pd; for Ag@Pt, the Pt shell compresses the Ag core (e_{core} = -3.98 % in the case of the Ih motif); inversely, for Pt@Ag with the same motif, the core expands (e_{core} = 2.59 %). For systems where the relative E_b of the composite elements are similar, there is significantly less strain present in the core and shell regions of the nanoparticle, hence the clustering of points where $e_{core} \approx e_{shell} \approx 0$.

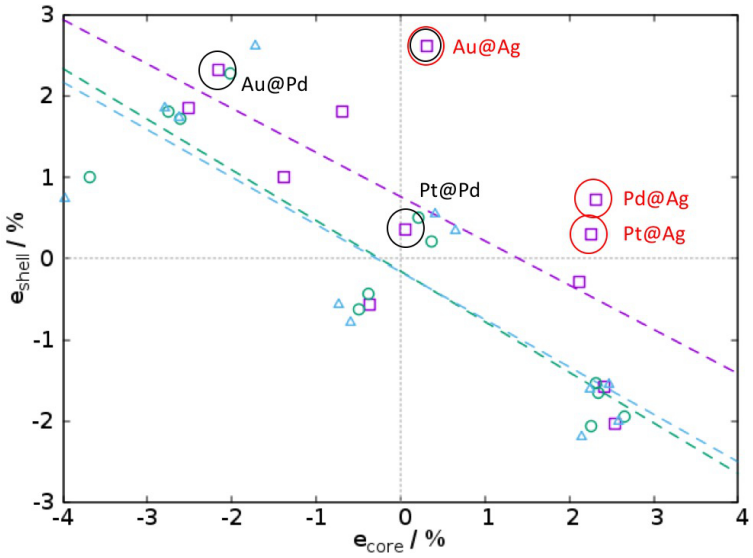

Figure 3: Relative strain on the core and shell atoms compared to the equivalent monometallic structures. Purple squares, green circles and blue triangles represent CO, I-Dh and Ih structural motifs, with the lines of best fit displayed as dashed lines as a guide to the eye. Significant outliers, namely CO structures with net positive strain, are highlighted in red, whilst CO structures that are the lowest energy motif for any composition are also highlighted in black.

3.2.2 Electronic Properties

The electronic properties of the bimetallic NPs have common trends: ε_f, ε_{HOMO} and ε_{LUMO} are defined by the element in the NP shell, agreeing with previous observations that ε_f is dependent on shell composition.[57] Presented in Table 2 are the values for ε_{HOMO} when considering the mono- and bimetallic Ih structures, with clear correlations visible in each column, indicating that the shell element dictates this particular electronic property. It is noted that for the weaker binding Ag, ε_{HOMO} decreases when stronger binding core elements are considered; and for the stronger binding

Pt, an inverse correlation is observed i.e. ε_{HOMO} decreases as weaker binding core elements are considered.

To illustrate further our point that nanoparticle properties depend heavily on the shell element, Figure 4 compares the density of states (DOS) when considering an NP composed either as Ag@M and M@Ag. For the Ag@M composition, ε_f is clearly varied and the DOS outline for the Ag, Au, Pd and Pt cores show little similarity, even if alligned to match by ε_f. In contrast, the consistent level in ε_f for all M@Ag NPs is clearly visible in the lower graph of Figure 4, allowing us to assert that the electronic properties are dominated by the shell element. Overall, ε_{HOMO} varies by only 0.07 eV for M@Ag; variation of 0.26 and 0.27 eV is noted for M@Au and M@Pt, which is attributed to the implicit strain of geometry and chemical variation. Furthermore, the lowest and highest ε_{HOMO} for M@Pt are when M = Ag and Pt, respectively, which correlates not only with binding energy, as noted above, but also with the Φ of the core metal (SI, Figure S4).The gap between occupied and unoccupied states, ε_g, is $\approx$ 0 eV for all NPs, with a greatest value of 0.06 eV for Ih Pd@Ag and 0.03 eV for Ih Pd@Au.

Table 2: Energy of the highest occupied molecular orbital (ε_{HOMO}) for monometallic and bimetallic core@shell NP structures. The element in the core (shell) of the NP is presented on the left (top). The values shown are for the Ih motif; full results are available in the SI for the I-Dh and CO motifs, with the range of values greatest for Ag@M, and at most 0.22 eV for Ag@Pt.

	Ag	Au	Pd	Pt
Ag	-4.05	-4.67	-4.99	-5.63
Au	-4.03	-4.83	-4.95	-5.59
Pd	-4.12	-4.96	-4.89	-5.46
Pt	-4.12	-4.83	-4.78	-5.36

The centre of mass for the d-band states was calculated for core ($\bar{\varepsilon}^d_{core}$) and shell ($\bar{\varepsilon}^d_{shell}$) atoms and is presented in Table 3. The energetic position in each case (core or shell) depends heavily on the elemental species, ranging for $\bar{\varepsilon}^d_{shell}$ over -3.87 to -4.10 (0.33), -3.21 to -3.55 (0.34), -1.46 to -1.79 (0.33) and -1.84 to -2.28 (0.44) eV for Ag, Au, Pd and Pt, respectively, with the overall variation given in brackets. These values are noted as being alignments with respect to ε_{HOMO}, in common with previous slab models, and when aligned absolutely the range of $\bar{\varepsilon}^d_{shell}$ is actually

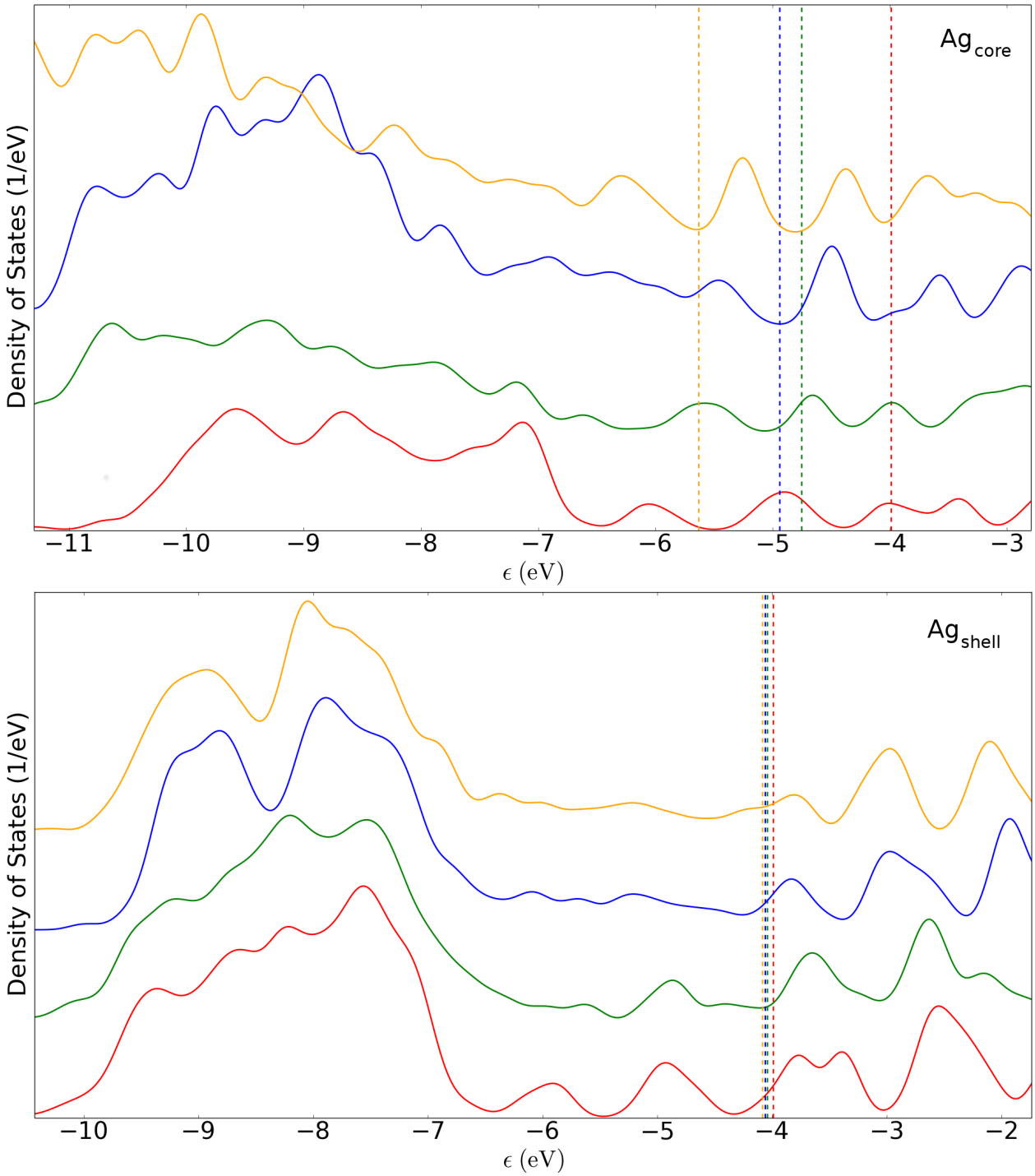

Figure 4: Projected density of states (PDOS) for Ag containing core@shell NPs. Top: PDOS for Ag atoms in the 55-atom core of a 147-atom Ih structure, with a 92-atom shell composed of Ag (red), Au (green), Pd (blue) and Pt (yellow). Bottom: PDOS for Ag atoms in the 92-atom shell of a 147-atom Ih structure, with a 55-atom core composed of Ag (red), Au (green), Pd (blue) and Pt (yellow). For clarity, the PDOS of each composition are offset by a constant in the y-axis and, in both graphs, the corresponding Fermi energy, ε_f, is given with vertical dashed line of the matching colour.

smaller: 0.26, 0.11, 0.21 and 0.28 eV for Ag, Au, Pd and Pt, respectively.

Table 3: Centre of mass for the occupied d-states ($\bar{\varepsilon}^d$) for monometallic and bimetallic core@shell NP structures.The element in the core (shell) of the NP is presented on the left (top) of each Table. The values are for the Ih geometry; full results for all structural motifs are available in the SI. For $\bar{\varepsilon}^d_{shell}$, the change relative to the monometallic system is given in brackets to aid comparison with literature.

$\bar{\varepsilon}^d$	Ag	Au	Pd	Pt
Ag:	-4.22	-3.92	-2.46	-2.80
Au:	-4.06	-3.62	-2.28	-2.60
Pd:	-3.19	-2.80	-1.97	-2.40
Pt:	-3.46	-3.18	-2.28	-2.67

$\bar{\varepsilon}^d_{core}$	Ag	Au	Pd	Pt
Ag:	-4.42	-4.54	-4.14	-4.30
Au:	-4.01	-4.00	-3.70	-3.87
Pd:	-2.06	-2.12	-2.43	-2.65
Pt:	-2.67	-2.84	-3.11	-3.31

$\bar{\varepsilon}^d_{shell}$	Ag	Au	Pd	Pt
Ag:	-4.10	-3.55	-1.46	-1.90
		(-0.15)	(0.24)	(0.38)
Au:	-4.09	-3.40	-1.43	-1.84
	(0.01)		(0.27)	(0.44)
Pd:	-3.87	-3.21	-1.70	-2.25
	(0.23)	(0.19)		(0.03)
Pt:	-3.93	-3.38	-1.79	-2.28
	(0.17)	(0.02)	(-0.09)	

Considering our observations alongside the slab calculations of Ruban *et al.*, our results for monometallic systems clearly match the previous work, with differences of 0.20, 0.16, 0.13 and -0.03 eV for $\bar{\varepsilon}^d_{shell}$; however, whilst qualitative agreement is found with experiment, quantitative disagreements are noted in comparison to the XPS measurements of transition metal foils by Hofmann *et al.*, who observed similar differences between computation and experiment themselves, and associated errors with underlying physical faults in DFT;[44] given that our results for monometallic systems are similar to those previously reported, we direct the reader to this previous work for a more thorough discussion of the monometallic systems.

In the case of bimetallic NPs, we again compare our results to the fixed slabs of Ruban *et*

al., where a monolayer "shell" of second species was included over a slab "core".[49] The relative changes in $\bar{\varepsilon}^{d}_{shell}$ (Table 3) are similar in magnitude for both ours and previous work, but there is an absence of consistent direction of shifts for the d-band centre in the slab and NP models: different signs are observed for Au@Ag (-0.21 vs. 0.01 eV in our work), Pd@Au (0.12 vs -0.15 eV), Au@Pd (-0.21 vs 0.27 eV), Pt@Pd (0.37 vs -0.09 eV) and Au@Pt (-0.08 vs 0.44 eV). We note a common theme exists for Au cores, where slab models give a positive (negative) d-band shift for Ag (Pd,Pt) shells, and the inverse occurs in our NP calculations. Furthermore, Gorzkowski and Lewera comment that a small decrease in $\bar{\varepsilon}^{d}$ is expected for NPs relative to slabs and bulk, due to size effects resulting in a decrease of ε_{HOMO};[55] however, we do not observe such an effect. Considering also the results of Tang and Henkelman for 79-atom FCC M@Pd NPs,[54] positive shifts in the d-band centre are observed for M = Ag and Au, relative to the Pd@Pd system, with values of approximately 0.20 and 0.25 eV; this is very close to our results of 0.24 and 0.27 eV for Ih, leading us to believe that morphology effects may be minimal.

To understand where the electrons have localised in our NPs, we analyse the atomic charge in the NPs, which can be correlated with variation in e.g. reactivity for vertices, edges and faces. With respect to charge equlibration alone, the most important information is whether charge accumulates in the shell or the core of the NPs: the increased degrees of freedom at a surface will attract electrons away from the core, though this could be countered by a strongly electronegative core element. For example, charge transfer from Ag to Au is common in AuAg NPs as the Au (2.4) is more electronegative than Ag (1.9),[86,87] whereas the electronegativity of Pd and Pt, which is 2.2 in both cases, differs less compared to the Group 11 elements,[77] and thus charge transfer may be considered less of an energetic driving force.

Our results for charge transfer (Table 4) have clear trends: for Ag@M, the core has significant charge depletion ($\bar{q}_{core} > 0$ e/atom), for all bimetallic NPs, with charge accumulation on the surfaces ($\bar{q}_{shell} < 0$ e/atom) and particularly the vertex sites (SI). Furthermore, for an Ag shell (M@Ag), charge transfer is also to the second element, indicating that, for the Ag containing NPs, the low electronegativity is more influential than surface effects. For cores of Au, Pd and Pt, charge

Table 4: Mean change in the electron density for the core ($\bar{q}_{core}$) and shell ($\bar{q}_{shell}$) atoms in monometallic and bimetallic core@shell NP structures. The element in the core (shell) of the NP is presented on the left (top). The values shown are for the Ih motif, with full results for all structures available in the SI.

$\bar{q}_{core}$	Ag	Au	Pd	Pt
Ag:	-0.03	-0.12	-0.10	-0.16
Au:	0.06	-0.05	-0.01	-0.08
Pd:	0.04	-0.05	-0.04	-0.10
Pt:	0.09	-0.03	-0.00	-0.07

$\bar{q}_{shell}$	Ag	Au	Pd	Pt
Ag:	0.06	0.11	0.07	0.14
Au:	0.02	0.09	0.05	0.12
Pd:	0.02	0.09	0.07	0.13
Pt:	0.03	0.09	0.07	0.14

transfer is towards the shell in all cases ($\bar{q}_{shell} > 0$ e/atom) with the Pt shell for M@Pt proving most prolific at accumulating charge. The outcome illustrates that the electronic degrees of freedom at the surface play an important role in charge localisation for the bimetallic NPs when the elements have similar electronegativities.

Referring back to the work of Tang and Henkelman, charge depletion was observed at the surface for Ag@Pd and Au@Pd, which may be related to strain effects in the FCC motif,[54] though no such effects were noted for our FCC fragment (CO) nor the I-Dh motif (SI). In contrast, we do observe similar results to Holmberg *et al.*: 0.05 and 0.07 e/atom are transferred to the surface for Au@Ag and Ag@Au, respectively. However, they also note the charge depletion from the core is inhomogeneous in the latter case, being predominantly from the subsurface layer, which may have some relation to the results we observe for an Ag core. In our simulations, the charge mostly accumulates at the NPs vertices (Figure 5), which we attribute to the lower coordination of these sites compared to edge and surface atoms; this trend is consistent for the Ih, I-Dh and CO structures (SI). We also note the variation in charge of the surface atoms for Figure 5A and Figure 5B, which is attributed to the breaking of symmetry in the structure geometry during the preceding structural optimisation.

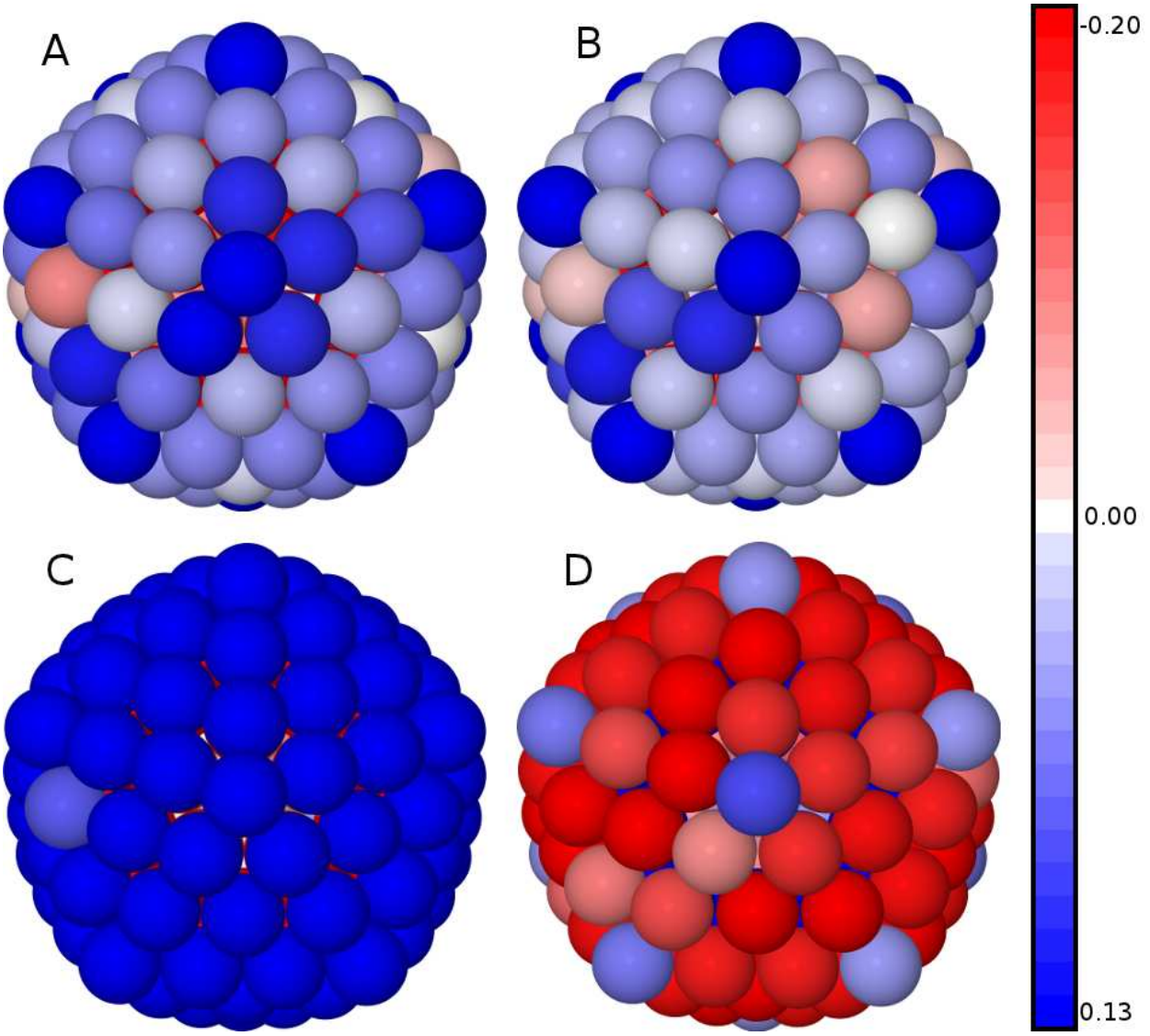

Figure 5: Schematic representation of charge localisation for: (A) Au; (B) Ag; (C) Ag@Au; and (D) Au@Ag 147-atom Ih NPs. Atoms highlighted in blue indicate those that have accummulated electrons due to charge transfer, and atoms highlighted in red mark atoms that have lost electron density; a scale is provided on the right hand side to aid the reader. Similar results were observed for I-Dh and CO structures (See SI).

4 Discussion

Previous work has highlighted clearly the correlation between the d-band centre and adsorption strength very clear for monometallic systems;[39–44] however, the inhomogeneous distribution of the constituent elements in bimetallic NPs, such as the case of core@shell segregation, means this standard model needs adaptation. The more complex parameter space, which now includes interfacial strain and charge transfer effects, is most obvious when considering the inconsistencies between our results and the previous slab calculations of Ruban *et al.*. However, our results do show that the general behaviour of d-band centres on NPs is as for slab surfaces, which implies that adsorption strength must be in-part correlated to the energetic position of the d-electrons on the *surface* atoms, rather than the same measurements for the entire NP. This is most clearly seen by noting the limited range of $\bar{\varepsilon}^{d}_{shell}$ in comparison to $\bar{\varepsilon}^{d}_{core}$ for the precious-metal elements discussed in this manuscript.

With this in mind, we now consider the report of Gorzkowski and Lewera,[55] where $\bar{\varepsilon}^{d}$ was measured as being particularly low for Pt@Pd NPs (-2.61 eV) and the previous computational results were labelled erroneous because of an absence of a downshift in $\bar{\varepsilon}^{d}_{shell}$. From our results in Table 3, we see that there *is* a downshift if we consider the d-band centre of the entire NP, $\bar{\varepsilon}^{d}$, as might be measured via XPS; however, the d-band states on the surface are higher than for the Pt core. Thus, our simulations differentiate between core and shell atoms, whereas the reported experiment does not appear to do so. In addtion, we also note that the monometallic results from Gorzkowski and Lewera, of -2.02 and -2.80 eV for Pd and Pt, are in very good agreement with our $\bar{\varepsilon}^{d}$ results of -1.97 and -2.67 eV.

Similarly, let us consider the results of Tedsree *et al.*[56] for M@Pd, where higher reactivity is attributed to a smaller work function for the core metal and the d-band model does not given a similar linear correlation. We do not disagree with the observations for the work function, which are matched in our results, but we also observe that Ag@Pd has a relatively low $\bar{\varepsilon}^{d}_{core}$, and this increases for Au@Pd and Pt@Pd. Thus, the effects we observe can be related to interfacial charge transfer effects, which are then dependent on the inherent material workfunctions. Additionally,

though, we note that $\bar{\varepsilon}^d_{shell}$ is relatively static in all our calculations, which implies other driving forces may be worth considering for the surface chemistry observed in experiment.

As a final observation, we look in more detail at the role of strain on the change of NP properties. As seen in Figure 6, little to no absolute change is observed for $\bar{\varepsilon}^d_{shell}$, or ε_{HOMO} (SI, Figure S5), due to the strain on the surface elements when changing the core element. In contrast, strain has more varied outcomes for the core elements: $\bar{\varepsilon}^d_{core}$ shifts by a considerable amount relative to the monometallic NP. Thus, further work is needed to systematically investigate these effects in the regime that is beyond that of quantum confinement ($N < 100$) whilst not yet at the bulk, as it seems the behaviour remains unpredictable at these sizes. Open questions remain with respect to the role of strain and whether such effects could be harnessed for monolayer metallic deposition on inorganic substrates, thus resulting in a shift of the d-band centre. We will investigate this in our future work.

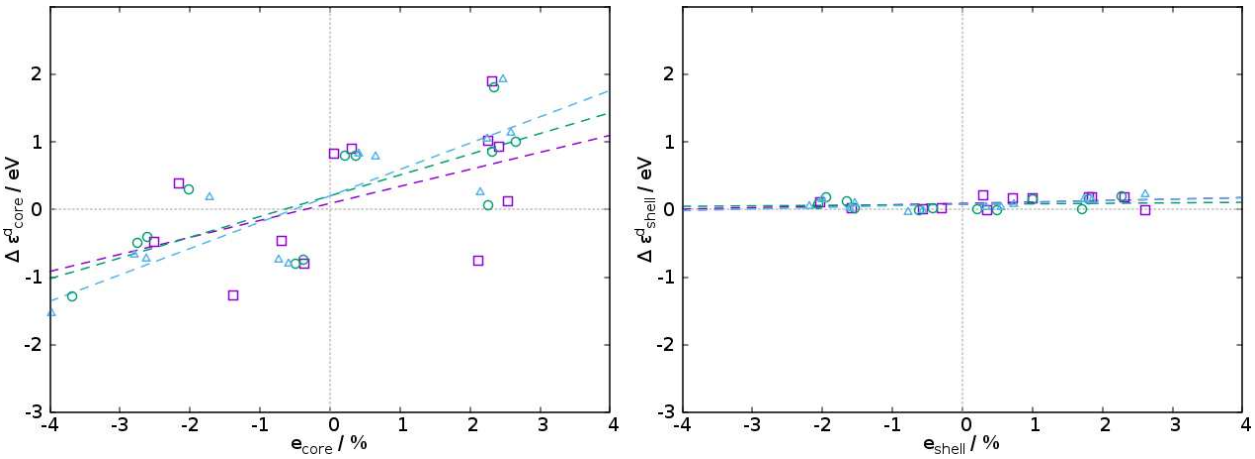

Figure 6: Strain for the core and shell elements relative to $\Delta\varepsilon^d$ for different structures, i.e. the change relative to monometallic NPs. $\Delta\varepsilon^d_{shell}$ is given in absolute terms, thus implicitly incorporating changes in the ε_{HOMO}. Purple squares, green circles and blue triangles represent CO, I-Dh and Ih structural motifs, with the lines of best fit displayed as dashed lines as a guide to the eye. The poor quality of the fit is illutrated by the R^2 of the fitted lines, which, for the core atoms, are 0.25, 0.56 and 0.74 for the CO, I-Dh and Ih, respectively; for the shell atoms, the R^2 of the fitted lines are 0.13, 0.02 and 0.26 for the same structures

5 Conclusions

We have investigated the structural, energetic and electronic properties of bimetallic NPs composed of the precious-metal elements Ag, Au, Pd and Pt, focusing specifically on the properties of core@shell nanostructures. The energetic properties are strongly correlated with the cohesive energy of the composite elements, with most compositions favouring the Ih structure for the 147-atom motifs investigated. Three specific chemical arrangements are more stable in a CO structure at this nuclearity, namely Au@Ag, Au@Pd and Pt@Pd. For Au@Pd, the compressed nature of the internal bonds in an Ih destabilises this motif relative to the CO, whereas perhaps such a structural preference is not observed for Au@Pt due to the greater strength of the encapsulating Pt-Pt bonds. For Au@Ag and Pt@Pd, the considered elements have similar radii but the stronger binding element is also at the core of the structure, and thus we conclude that an ideal bond length for this element, as facilitated by the FCC motif, ensures that the overall binding of the CO NP is stronger than the more compressed Ih.

Analysis of the electronic structure shows that the energy of the highest occupied molecular orbitals (ε_{HOMO}) is strongly correlated to the element in the shell of the NP, with minor variance depending on the core. ε_{HOMO} is lowest for systems with a Pt shell, and increases when Pt is replaced by Pd, Au and Ag, respectively. For Ag@M, an energy gap in the electronic levels is identified, which is also seen for Au@Au and Pd@Au; no energy gap is seen for systems with Pd or Pt shells. Further review of the DOS offers insight into the positioning of the d-band centre of mass, which plays an important part in the generic concepts of bonding during catalytic reactions. The centre of mass for shell-centred d-band electrons is fairly consistent irrespective of the element in the core of the NP, with ranges relative to ε_{HOMO} of 0.23, 0.34, 0.36 and 0.44 eV for shells of Ag, Au, Pd and Pt, respectively; and only 0.33, 0.07, 0.16 and 0.11 eV in absolute terms. This observation is extremely important as these are the physically accessible states for interacting adsorbate molecules. Finally, we analysed the charge segregation across the NPs. In general electrons accumulate at the NP surfaces irrespective of the core@shell composition, except in the case of Ag: for M@Ag the core tends to gain electron density, which is explained due to the

low electronegativity of Ag (1.9) with respect to other constituent elements (Au: 2.4; Pd: 2.2; Pt: 2.2). In all cases charge accumulates more prominently on the vertices of the NPs, especially for Pt surfaces, and less so on the edges and surfaces, showing a distinct correlation between coordination number and charge accumulation.

Supporting Information Available

The Supporting Information contains thorough analysis of the structure, energetic and electronic properties for nanoparticles considered in this study, Tables of data containing all reported observables for the bimetallic nanoparticles discussed in this article, and Graphs of: (i) the projected density of states for NPs with a Pt shell and varying core elements; and (ii) the relationship between strain and the change in the position of ε_{HOMO}. This material is available free of charge via the Internet at http://pubs.acs.org. Information on the data underpinning the results presented here, including how to access them, can be found in the Cardiff University data catalogue at http://doi.org/10.17035/d.2018.0045513133

Acknowledgement

The authors acknowledge N. Dimitratos, D. O. Scanlon, A. A. Sokol and C. R. A. Catlow for several stimulating and useful conversations. Via our membership of the UK's HEC Materials Chemistry Consortium, which is funded by EPSRC (EP/L000202), this work used the ARCHER UK National Supercomputing Service. This work also used the computational facilities of the Advanced Research Computing @ Cardiff (ARCCA) Division, Cardiff University.

References

1. Haruta, M.; Tsubota, S.; Kobayashi, T.; Kageyama, H.; Genet, M. J.; Delmon, B. Low-Temperature Oxidation of CO over Gold Supported on TiO_2, α-Fe_2O_3, and Co_3O_4. *J. Catal.* **1993**, *144*, 175–192.

2. Hutchings, G. Vapor phase hydrochlorination of acetylene: Correlation of catalytic activity of supported metal chloride catalysts. *J. Catal.* **1985**, *96*, 292 – 295.

3. Haruta, M.; Daté, M. Advances in the Catalysis of Au Nanoparticles. *Appl. Catal. A: Gen.* **2001**, *222*, 427 – 437.

4. Turner, M.; Golovko, V. B.; Vaughan, O. P.; Abdulkin, P.; Berenguer-Murcia, A.; Tikhov, M. S.; Johnson, B. F.; Lambert, R. M. Selective oxidation with dioxygen by gold nanoparticle catalysts derived from 55-atom clusters. *Nature* **2008**, *454*, 981–983.

5. Corma, A.; Garcia, H. Supported gold nanoparticles as catalysts for organic reactions. *Chemical Society Reviews* **2008**, *37*, 2096–2126.

6. Hvolbæk, B.; Janssens, T. V.; Clausen, B. S.; Falsig, H.; Christensen, C. H.; Nørskov, J. K. Catalytic activity of Au nanoparticles. *Nano Today* **2007**, *2*, 14–18.

7. Narayanan, R.; El-Sayed, M. A. Shape-dependent catalytic activity of platinum nanoparticles in colloidal solution. *Nano letters* **2004**, *4*, 1343–1348.

8. Wilson, O. M.; Knecht, M. R.; Garcia-Martinez, J. C.; Crooks, R. M. Effect of Pd nanoparticle size on the catalytic hydrogenation of allyl alcohol. *Journal of the American Chemical Society* **2006**, *128*, 4510–4511.

9. Huang, D.; Liao, F.; Molesa, S.; Redinger, D.; Subramanian, V. Plastic-compatible low resistance printable gold nanoparticle conductors for flexible electronics. *Journal of the electrochemical society* **2003**, *150*, G412–G417.

10. Li, Y.; Wu, Y.; Ong, B. S. Facile synthesis of silver nanoparticles useful for fabrication of high-conductivity elements for printed electronics. *Journal of the American Chemical Society* **2005**, *127*, 3266–3267.

11. Takei, K.; Yu, Z.; Zheng, M.; Ota, H.; Takahashi, T.; Javey, A. Highly sensitive electronic whiskers based on patterned carbon nanotube and silver nanoparticle composite films. *Proceedings of the National Academy of Sciences* **2014**, *111*, 1703–1707.

12. Elghanian, R.; Storhoff, J. J.; Mucic, R. C.; Letsinger, R. L.; Mirkin, C. A. Selective colorimetric detection of polynucleotides based on the distance-dependent optical properties of gold nanoparticles. *Science* **1997**, *277*, 1078–1081.

13. Haynes, C. L.; Van Duyne, R. P. Nanosphere lithography: a versatile nanofabrication tool for studies of size-dependent nanoparticle optics. *The Journal of Physical Chemistry B* **2001**, *105*, 5599–5611.

14. Kelly, K. L.; Coronado, E.; Zhao, L. L.; Schatz, G. C. The Optical Properties of Metal Nanoparticles: The Influence of Size, Shape, and Dielectric Environment. *J. Phys. Chem. B* **2003**, *107*, 668–677.

15. Toshima, N.; Yonezawa, T. Bimetallic nanoparticles—novel materials for chemical and physical applications. *New Journal of Chemistry* **1998**, *22*, 1179–1201.

16. Nanoalloys: From Theory to Applications. *Faraday Discussions No.138*, 2008.

17. Ferrando, R.; Jellinek, J.; Johnston, R. L. Nanoalloys: From Theory to Applications of Alloy Clusters and Nanoparticles. *Chem. Rev.* **2008**, *108*, 845–910.

18. Johnston, R. L.; Wilcoxon, J. P. *Metal Nanoparticles and Nanoalloys*; Frontiers of Nanoscience (Vol. 3); Elsevier: Oxford, 2012.

19. Sau, T. K.; Murphy, C. J. Room temperature, high-yield synthesis of multiple shapes of gold

nanoparticles in aqueous solution. *Journal of the American Chemical Society* **2004**, *126*, 8648–8649.

20. Wegner, K.; Piseri, P.; Tafreshi, H. V.; Milani, P. Cluster beam deposition: a tool for nanoscale science and technology. *Journal of Physics D: Applied Physics* **2006**, *39*, R439.

21. Su, R.; Tiruvalam, R.; Logsdail, A. J.; He, Q.; Downing, C. A.; Jensen, M. T.; Dimitratos, N.; Kesavan, L.; Wells, P. P.; Bechstein, R. et al. Designer titania-supported Au–Pd nanoparticles for efficient photocatalytic hydrogen production. *ACS nano* **2014**, *8*, 3490–3497.

22. Sankar, M.; Dimitratos, N.; Miedziak, P. J.; Wells, P. P.; Kiely, C. J.; Hutchings, G. J. Designing bimetallic catalysts for a green and sustainable future. *Chem. Soc. Rev.* **2012**, *41*, 8099–8139.

23. Strasser, P.; Koh, S.; Anniyev, T.; Greeley, J.; More, K.; Yu, C.; Liu, Z.; Kaya, S.; Nordlund, D.; Ogasawara, H. et al. Lattice-strain control of the activity in dealloyed core–shell fuel cell catalysts. *Nature Chem.* **2010**, *2*, 454–460.

24. Villa, A.; Dimitratos, N.; Chan-Thaw, C. E.; Hammond, C.; Prati, L.; Hutchings, G. J. Glycerol Oxidation Using Gold-Containing Catalysts. *Accounts of chemical research* **2015**, *48*, 1403–1412.

25. Alayoglu, S.; Nilekar, A. U.; Mavrikakis, M.; Eichhorn, B. Ru-Pt core-shell nanoparticles for preferential oxidation of carbon monoxide in hydrogen. *Nature Mater.* **2008**, *7*, 333–338.

26. Johnston, R. L. Evolving better nanoparticles: Genetic algorithms for optimising cluster geometries. *Dalton Trans.* **2003**, 4193.

27. Ferrando, R.; Fortunelli, A.; Johnston, R. L. Searching for the optimum structures of alloy nanoclusters. *Chem. Phys. Phys. Chem.* **2008**, *10*, 640–649.

28. Paz-Borbón, L. O.; Johnston, R. L.; Barcaro, G.; Fortunelli, A. Structural motifs, mixing, and segregation effects in 38-atom binary clusters. *J. Chem. Phys.* **2008**, *128*, 134517.

29. Rapallo, A.; Rossi, G.; Ferrando, R.; Fortunelli, A.; Curley, B. C.; Lloyd, L. D.; Tarbuck, G. M.; Johnston, R. L. Global optimization of bimetallic cluster structures. I. Size-mismatched Ag–Cu, Ag–Ni, and Au–Cu systems. *The Journal of chemical physics* **2005**, *122*, 194308.

30. Rossi, G.; Ferrando, R.; Rapallo, A.; Fortunelli, A.; Curley, B. C.; Lloyd, L. D.; Johnston, R. L. Global optimization of bimetallic cluster structures. II. Size-matched Ag-Pd, Ag-Au, and Pd-Pt systems. *The Journal of chemical physics* **2005**, *122*, 194309.

31. Kozlov, S. M.; Kovacs, G.; Ferrando, R.; Neyman, K. M. How to determine accurate chemical ordering in several nanometer large bimetallic crystallites from electronic structure calculations. *Chem. Sci.* **2015**, *6*, 3868–3880.

32. Scamehorn, C. A.; Harrison, N. M.; McCarthy, M. I. Water chemistry on surface defect sites: Chemidissociation versus physisorption on MgO(001). *J. Chem. Phys.* **1994**, *101*, 1547–1554.

33. Jennings, P. C.; Pollet, B. G.; Johnston, R. L. Electronic Properties of Pt–Ti Nanoalloys and the Effect on Reactivity for Use in PEMFCs. *J. Phys. Chem. C* **2012**, *116*, 15241–15250.

34. Jennings, P.; Aleksandrov, H.; Neyman, K.; Johnston, R. O2 Dissociation on M@Pt Core–Shell Particles for 3d, 4d, and 5d Transition Metals. *J. Phys. Chem. C* **2015**, *119*, 11031–11041.

35. Song, C.; Ge, Q.; ; Wang*, L. DFT Studies of Pt/Au Bimetallic Clusters and Their Interactions with the CO Molecule. *The Journal of Physical Chemistry B* **2005**, *109*, 22341–22350, PMID: 16853910.

36. Nilekar, A. U.; Alayoglu, S.; Eichhorn, B.; Mavrikakis, M. Preferential CO Oxidation in Hydrogen: Reactivity of CoreâĹŠShell Nanoparticles. *Journal of the American Chemical Society* **2010**, *132*, 7418–7428, PMID: 20459102.

37. Roldán, A.; Viñes, F.; Illas, F.; Ricart, J.; Neyman, K. M. Density functional studies of coinage metal nanoparticles: scalability of their properties to bulk. *Theor. Chem. Acc.* **2008**, *120*, 565–573.

38. Yudanov, I. V.; Genest, A.; Rösch, N. DFT Studies of Palladium Model Catalysts: Structure and Size Effects. *J. Clust. Sci* **2011**, *22*, 433–448.

39. Hammer, B.; Nørskov, J. Electronic factors determining the reactivity of metal surfaces. *Surface Science* **1995**, *343*, 211–220.

40. Nørskov, J. K.; Bligaard, T.; Rossmeisl, J.; Christensen, C. H. Towards the computational design of solid catalysts. *Nature Chem.* **2009**, *1*, 37–46.

41. Nørskov, J. K.; Abild-Pedersen, F.; Studt, F.; Bligaard, T. Density functional theory in surface chemistry and catalysis. *Proceedings of the National Academy of Sciences* **2011**, *108*, 937–943.

42. Crampton, A. S.; Rötzer, M. D.; Schweinberger, F. F.; Yoon, B.; Landman, U.; Heiz, U. Ethylene hydrogenation on supported Ni, Pd and Pt nanoparticles: Catalyst activity, deactivation and the d-band model. *Journal of Catalysis* **2016**, *333*, 51 – 58.

43. Lima, F. H. B.; Zhang, J.; Shao, M. H.; Sasaki, K.; Vukmirovic, M. B.; Ticianelli, E. A.; Adzic, R. R. Catalytic ActivityâĹŠd-Band Center Correlation for the O2 Reduction Reaction on Platinum in Alkaline Solutions. *The Journal of Physical Chemistry C* **2007**, *111*, 404–410.

44. Hofmann, T.; Yu, T. H.; Folse, M.; Weinhardt, L.; Bär, M.; Zhang, Y.; Merinov, B. V.; Myers, D. J.; Goddard, W. A.; Heske, C. Using Photoelectron Spectroscopy and Quantum Mechanics to Determine d-Band Energies of Metals for Catalytic Applications. *J. Phys. Chem. C* **2012**, *116*, 24016–24026.

45. Calle-Vallejo, F.; Loffreda, D.; Koper, M. T.; Sautet, P. Introducing structural sensitivity into

adsorption–energy scaling relations by means of coordination numbers. *Nature Chem.* **2015**, *7*, 403–410.

46. Calle-Vallejo, F.; Tymoczko, J.; Colic, V.; Vu, Q. H.; Pohl, M. D.; Morgenstern, K.; Loffreda, D.; Sautet, P.; Schuhmann, W.; Bandarenka, A. S. Finding optimal surface sites on heterogeneous catalysts by counting nearest neighbors. *Science* **2015**, *350*, 185–189.

47. Paz-Borbón, L.; Baletto, F. A DFT Study on the O2 Adsorption Properties of Supported PtNi Clusters. *Inorganics* **2017**, *5*, 43.

48. Mott, D.; Luo, J.; Njoki, P. N.; Lin, Y.; Wang, L.; Zhong, C.-J. Synergistic activity of gold-platinum alloy nanoparticle catalysts. *Catal. Today* **2007**, *122*, 378 – 385.

49. Ruban, A.; Hammer, B.; Stoltze, P.; Skriver, H. L.; Nørskov, J. K. Surface electronic structure and reactivity of transition and noble metals. *J. Mol. Catal. A Chem.* **1997**, *115*, 421–429.

50. Greeley, J.; Nørskov, J. K. A general scheme for the estimation of oxygen binding energies on binary transition metal surface alloys. *Surface Science* **2005**, *592*, 104 – 111.

51. Kibler, L. A.; El-Aziz, A. M.; Hoyer, R.; Kolb, D. M. Tuning reaction rates by lateral strain in a palladium monolayer. *Angewandte Chemie International Edition* **2005**, *44*, 2080–2084.

52. Pedersen, M.; Helveg, S.; Ruban, A.; Stensgaard, I.; Lægsgaard, E.; Nørskov, J.; Besenbacher, F. How a gold substrate can increase the reactivity of a Pt overlayer. *Surf. Sci.* **1999**, *426*, 395–409.

53. Roudgar, A.; Groß, A. Local reactivity of metal overlayers: Density functional theory calculations of Pd on Au. *Phys. Rev. B* **2003**, *67*, 33409.

54. Tang, W.; Henkelman, G. Charge redistribution in core-shell nanoparticles to promote oxygen reduction. *J. Chem. Phys.* **2009**, *130*, 194504.

55. Gorzkowski, M.; Lewera, A. Probing the limits of d-band Center Theory: Electronic and Electrocatalytic Properties of Pd-Shell-Pt-Core Nanoparticles. *J. Phys. Chem. C* **2015**, *119*, 18389–18395.

56. Tedsree, K.; Li, T.; Jones, S.; Chan, C. W. A.; Yu, K. M. K.; Bagot, P. A. J.; Marquis, E. A.; Smith, G. D. W.; Tsang, S. C. E. Hydrogen production from formic acid decomposition at room temperature using a Ag-Pd core-shell nanocatalyst. *Nat Nano* **2011**, *6*, 302–307.

57. Holmberg, N.; Laasonen, K.; Peljo, P. Charge distribution and Fermi Level in bimetallic nanoparticles. *Phys. Chem. Chem. Phys.* **2016**, *18*, 2924–2931.

58. Vegard, L. Die konstitution der mischkristalle und die raumfüllung der atome. *Zeitschrift für Physik A Hadrons and Nuclei* **1921**, *5*, 17–26.

59. Martin, T. P. Shells of atoms. *Phys. Rep.* **1996**, *273*, 199–241.

60. Johnston, R. L. *Atomic and Molecular Clusters*; Taylor and Francis: London, 2002.

61. Baletto, F.; Ferrando, R.; Fortunelli, A.; Montalenti, F.; Mottet, C. Crossover among structural motifs in transition and noble-metal clusters. *J. Chem. Phys.* **2002**, *116*, 3856–3863.

62. Xing, X.; Yoon, B.; Landman, U.; Parks, J. H. Structural Evolution of Au Nanoclusters: From Planar to Cage to Tubular Motifs. *Phys. Rev. B* **2006**, *74*, 165423.

63. Baletto, F.; Ferrando, R. Structural properties of nanoclusters: Energetic, thermodynamic, and kinetic effects. *Rev. Mod. Phys.* **2005**, *77*, 371–423.

64. Li, Z. Y.; Young, N. P.; Vece, M. D.; Palomba, S.; Palmer, R. E.; Bleloch, A. L.; Curley, B. C.; Johnston, R. L.; Jiang, J.; Yuan, J. Three-dimensional Atomic-scale Structure of Size-selected Gold Nanoclusters. *Nature* **2008**, *451*, 46–48.

65. Wells, D. M.; Rossi, G.; Ferrando, R.; Palmer, R. E. Metastability of the atomic structures of size-selected gold nanoparticles. *Nanoscale* **2015**, *7*, 6498–6503.

66. Tozer, D. J.; De Proft, F. Computation of the Hardness and the Problem of Negative Electron Affinities in Density Functional Theory. *J. Phys. Chem. A* **2005**, *109*, 8923–8929, PMID: 16834296.

67. Yu, W. W.; Wang, Y. A.; ; Peng*, X. Formation and Stability of Size-, Shape-, and Structure-Controlled CdTe Nanocrystals:âĂL' Ligand Effects on Monomers and Nanocrystals. *Chemistry of Materials* **2003**, *15*, 4300–4308.

68. T. Rajh, .; Chen, L. X.; Lukas, K.; Liu, T.; Thurnauer, M. C.; ; Tiede, D. M. Surface Restructuring of Nanoparticles:âĂL' An Efficient Route for LigandâĹŠMetal Oxide Crosstalk. *The Journal of Physical Chemistry B* **2002**, *106*, 10543–10552.

69. Mortensen, J. J.; Hansen, L. B.; Jacobsen, K. W. Real-space Grid Implementation of the Projector Augmented Wave Method. *Phys. Rev. B* **2005**, *71*, 035109.

70. Enkovaara, J.; Rostgaard, C.; Mortensen, J. J.; Chen, J.; Dulak, M.; Ferrighi, L.; Gavnholt, J.; Glinsvad, C.; Haikola, V.; Hansen, H. A. et al. Electronic Structure Calculations with GPAW: a Real-space Implementation of the Projector Augmented-wave Method. *J. Phys.: Condens. Matter* **2010**, *22*, 253202.

71. Blöchl, P. E. Projector Augmented-wave Method. *Phys. Rev. B* **1994**, *50*, 17953–17979.

72. Marchal, R.; Yudanov, I. V.; Matveev, A. V.; Rösch, N. Scalable properties of metal clusters: A comparative DFT study of ionic-core treatments. *Chem. Phys. Lett.* **2013**, *578*, 92–96.

73. Kresse, G.; Furthmüller, J. Efficient iterative schemes for *ab initio* total-energy calculations using a plane-wave basis set. *Phys. Rev. B* **1996**, *54*, 11169–11186.

74. Perdew, J. P.; Burke, K.; Ernzerhof, M. Generalized Gradient Approximation Made Simple. *Phys. Rev. Lett.* **1996**, *77*, 3865–3868.

75. Shanno, D. F. Conditioning of Quasi-Newton Methods for Function Minimization. *Math. Comp.* **1970**, *24*, 647–656.

76. Tang, W.; Sanville, E.; Henkelman, G. A Grid-based Bader Analysis Algorithm without Lattice Bias. *J. Phys.: Compute Mater.* **2009**, *21*, 084204.

77. Kittel, C. *Introduction To Solid State Physics* 8^{th} *Edition*; Wiley: New York, 2004.

78. Perdew, J. P.; Zunger, A. Self-interaction correction to density-functional approximations for many-electron systems. *Phys. Rev. B* **1981**, *23*, 5048–5079.

79. Zarechnaya, E. Y.; Skorodumova, N. V.; Simak, S.; Johansson, B.; Isaev, E. I. Theoretical study of linear monoatomic nanowires, dimer and bulk of Cu, Ag, Au, Ni, Pd and Pt. *Computational materials science* **2008**, *43*, 522–530.

80. Salzner, U.; Baer, R. Koopmans' springs to life. *J. Chem. Phys* **2009**, *131*, 231101.

81. Bellafont, N. P.; Illas, F.; Bagus, P. S. Validation of Koopmans' theorem for density functional theory binding energies. *Phys. Chem. Chem. Phys.* **2015**, *17*, 4015.

82. Lide, D. R. *CRC Handbook of Chemistry and Physics, 84th Edition*; CRC Press: Boca Raton, Florida, 2003.

83. Bochicchio, D.; Ferrando, R. Morphological instability of core-shell metallic nanoparticles. *Phys. Rev. B* **2013**, *87*, 165435.

84. Laasonen, K.; Panizon, E.; Bochicchio, D.; Ferrando, R. Competition between Icosahedral Motifs in AgCu, AgNi, and AgCo Nanoalloys: A Combined Atomistic–DFT Study. *The Journal of Physical Chemistry C* **2013**, *117*, 26405–26413.

85. Panizon, E.; Bochicchio, D.; Rossi, G.; Ferrando, R. Tuning the structure of nanoparticles by small concentrations of impurities. *Chemistry of Materials* **2014**, *26*, 3354–3356.

86. Gould, a. L.; Heard, C. J.; Logsdail, a. J.; Catlow, C. R. a. Segregation effects on the properties of (AuAg) 147. *Phys. Chem. Chem. Phys.* **2014**, *16*, 21049–21061.

87. Cerbelaud, M.; Ferrando, R.; Barcaro, G.; Fortunelli, A. Optimization of chemical ordering in AgAu nanoalloys. *Phys. Chem. Chem. Phys.* **2011**, *13*, 10232.

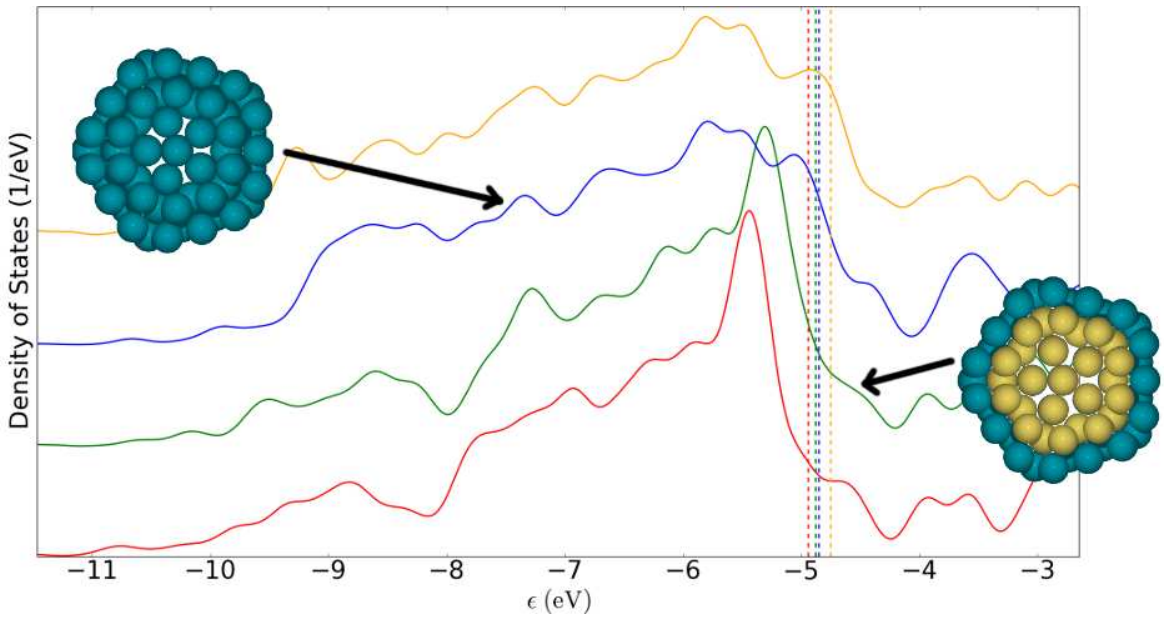

Figure 7: Graphic for Table of Contents

This material is available free of charge via the Internet at `http://pubs.acs.org/`.